

Thermal expansion of alunite up to dehydroxylation and collapse of the crystal structure

M. ZEMA^{1*}, A. M. CALLEGARI^{1,2}, S. C. TARANTINO¹, E. GASPARINI¹ AND P. GHIGNA³

¹ Dipartimento di Scienze della Terra e dell'Ambiente, Università di Pavia, via Ferrata 1, I-27100 Pavia, Italy

² Sistema Museale di Ateneo, Università di Pavia, Corso Strada Nuova 65, I-27100 Pavia, Italy

³ Dipartimento di Chimica, Università di Pavia, Viale Taramelli 16, I-27100 Pavia, Italy

[Received 11 January 2012; Accepted 8 March 2012; Associate Editor: Wilson Crichton]

ABSTRACT

The high-temperature (HT) behaviour of a sample of natural alunite was investigated by means of *in situ* HT single-crystal X-ray diffraction from room temperature up to the dehydroxylation temperature and consequent collapse of the crystal structure. In the temperature range 25–500°C, alunite expands anisotropically, with most of the contribution to volume dilatation being produced by expansion in the *c* direction. The thermal expansion coefficients determined over the temperature range investigated are: $\alpha_a = 0.61(2) \times 10^{-5} \text{ K}^{-1}$ ($R^2 = 0.988$), $\alpha_c = 4.20(7) \times 10^{-5} \text{ K}^{-1}$ ($R^2 = 0.996$), $\alpha_c/\alpha_a = 6.89$, $\alpha_v = 5.45(7) \times 10^{-5} \text{ K}^{-1}$ ($R^2 = 0.998$). At ~275–300°C, a minor discontinuity in the variation of unit-cell parameters with temperature is observed and interpreted on the basis of loss of H_3O^+ that partially substitutes for K^+ at the monovalent *A* site in the alunite structure. Increasing temperature causes the $\text{Al}(\text{O},\text{OH})_6$ sheets, which remain almost unaltered along the basal plane, to move further apart, and this results in an expansion of the coordination polyhedron around the intercalated potassium cation. Sulfate tetrahedra act as nearly rigid units, they contract a little in the lower temperature range to accommodate the elongation of the Al octahedra.

KEYWORDS: alunite, thermal expansion, single-crystal X-ray diffraction.

Introduction

ALUNITE, $\text{KAl}_3(\text{SO}_4)_2(\text{OH})_6$, is a common sulfate mineral in high-sulfidation hydrothermal systems and sedimentary environments (Stoffregen and Alpers, 1992; Dill, 2001). It is used as a raw material by the chemical industry to produce potash alum and alumina, which are typically obtained by calcination methods and subsequent extraction. Alunite has potential applications as a coagulant for water purification (Sengil, 1995) and as a cement additive due to its ability to adsorb phosphate from aqueous solution (Özacar, 2003; Katsioti *et al.*, 2005). In addition, alunite-type phases have been proposed as potential hosts

for the long-term immobilization of radioactive waste and toxic heavy metals (Ballhorn *et al.*, 1989; Kolitsch *et al.*, 1999).

Alunite is a member of the alunite group of minerals (Jambor, 1999; Mills *et al.*, 2009; Bayliss *et al.*, 2010). The minerals of this group have a general chemical formula $AR_3(\text{SO}_4)_2(\text{OH})_6$, where *A* typically contains twelve-coordinated K^+ and Na^+ (minerals and synthetic analogues where *A* is populated by Ag^+ , Ca^{2+} , NH_4^+ , Pb^{2+} and H_3O^+ are known), and *R* contains octahedrally coordinated Al or Fe^{3+} (if Fe^{3+} is the dominant component at *R*, the minerals belong to the jarosite group). Alunite-group minerals typically crystallize in the trigonal system in space group $R\bar{3}m$; although there are a few exceptions that require further research. Alunite was originally described by Hendricks (1937) in the acentric space group $R3m$ because

* E-mail: michele.zema@unipv.it
DOI: 10.1180/minmag.2012.076.3.12

of its pyroelectric properties. Wang *et al.* (1965) subsequently showed that alunite crystal structure is centrosymmetric and refined it in space group $R\bar{3}m$. All subsequent work (e.g. Menchetti and Sabelli, 1976; Schukow *et al.*, 1999; Stoffregen *et al.*, 2000; Majzlan *et al.*, 2006) has shown this to be correct.

The crystal structure of alunite is illustrated in Fig. 1. It consists of sheets of distorted corner-sharing $\text{Al}(\text{O},\text{OH})_6$ octahedra, each sharing all the OH groups (i.e. O3) in the basal plane to form large hexagonal and small trigonal rings (a kagome network) normal to the c axis (Fig. 1b). Three oxygen atoms (O2) from the apices of adjacent Al octahedra form the basal edges of sulfate tetrahedra, which are completed by one unshared apical oxygen atom (O1). The resulting arrangement allows the formation of large cavities, which are located between adjacent Al-bearing layers, where K^+ cations are hosted. Each potassium cation is coordinated by six OH groups from the Al octahedra and six oxygen atoms common to Al octahedra and S tetrahedra. Hydrogen atoms form weak hydrogen bonds

with the apical oxygen atoms of sulfate tetrahedra as acceptors (Schukow *et al.*, 1999).

The thermal decomposition of alunite has been studied since the early twentieth century (Fink *et al.*, 1931). Alunite undergoes a transformation to dehydrated potassium alum at $\sim 500^\circ\text{C}$ according to the following reaction:



which also produces highly reactive alumina. Further heating drives off sulfur, through different steps at $T > 800^\circ\text{C}$, to produce potassium oxide and gaseous SO_3 . Despite significant research the structural details of alunite at high temperature are not known. Xu *et al.* (2010) recently determined the thermal expansion coefficients for jarosite, the Fe^{3+} analogue of alunite, and gave a detailed analysis of its high temperature (HT) structure on the basis of *in situ* HT neutron powder diffraction. As far as we know, this is the only HT structural investigation of alunite-like minerals. The aim of the present work is to characterize the thermal behaviour of a natural alunite, from room temperature (RT) up to the collapse of the

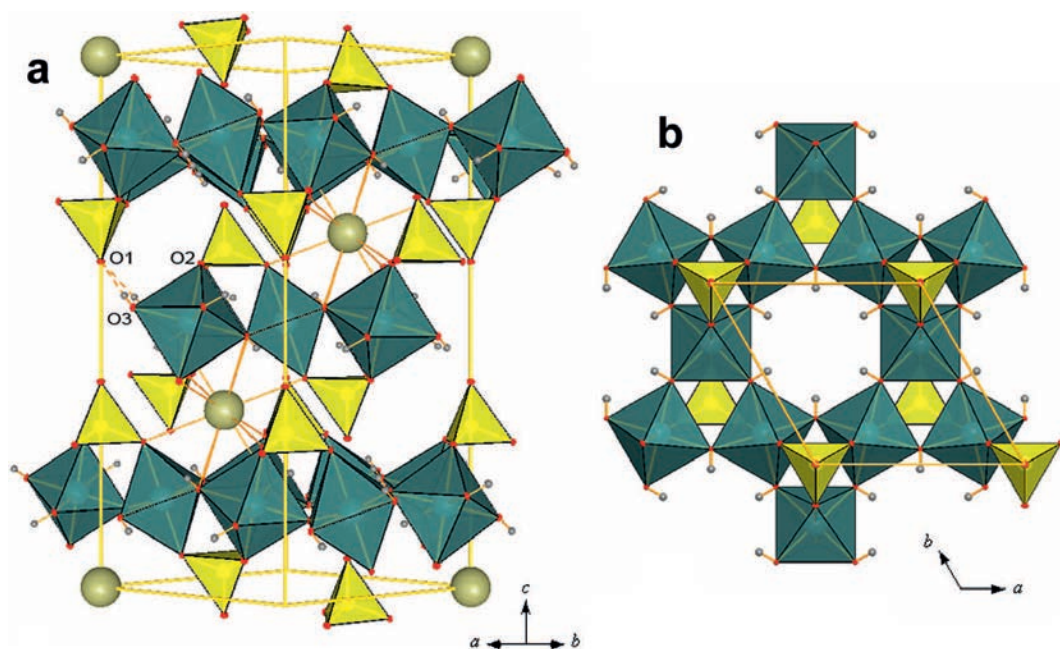


FIG. 1. (a) Perspective view of the crystal structure of alunite along $(11\bar{2}0)$. The Al octahedra (dark green) share all four basal oxygen atoms and protonated O3, to form layers along the (0001) plane, as depicted in (b) which shows apical oxygen atoms O2 shared with SO_4 tetrahedra (yellow), whose coordination shell is completed by unshared O1 oxygen atoms. The twelve-coordinated K^+ cations (gold) occupy large interlayer cavities between six O2 and six O3 oxygen atoms. Hydrogen atoms are shown in grey.

structure due to dehydroxylation, by *in situ* HT single-crystal X-ray diffraction.

Experimental

Sample

A transparent, grey, $0.16 \times 0.13 \times 0.12$ mm crystal of alunite from Hungary was selected for the X-ray diffraction measurements based on its optical and diffraction properties. The specimen was provided by the Mineralogical Museum of the University of Pavia (specimen no. 2696). The chemical composition of the sample is close to the ideal formula as revealed by energy dispersive X-ray analysis (EDS) on a scanning electron microscope (SEM) of the residual crystal at the end of the HT structural investigations. In the resulting dehydrated potash alum there is only minor substitution of Na for K (K:Na ratio ~10:1) and minor P present (<1%). Recalculation of the chemical formula based on eight oxygen atoms would indicate partial non-stoichiometry at the A site but the data are quite scattered due to cation migration and release of volatiles during exposure of the sample to the electron beam and the presence of nanometric Al_2O_3 , produced by dehydroxylation, which could be included in the spot analyses. By combining such information with the results of structure refinements and considerations of the thermal behaviour shown by the sample (see below), the chemical formula $[\text{K}_{0.88}\text{Na}_{0.07}(\text{H}_3\text{O})_{0.05}]\text{Al}_3(\text{SO}_4)_2(\text{OH})_6$ was derived for the untreated alunite sample.

Single-crystal XRD measurements

Both RT and *in situ* HT single-crystal diffraction investigations were carried out using a Philips PW1100 four-circle diffractometer with a point-counter detector. Operating conditions were 55 kV and 30 mA using graphite-monochromated $\text{MoK}\alpha$ radiation ($\lambda = 0.71073$ Å). The horizontal and vertical apertures were 2.0 and 1.5°, respectively. For the HT measurements, the crystal was inserted into a quartz capillary (0.3 mm in diameter) and held in position by means of quartz wool and heated in a custom-made U-shaped micro-furnace with a K-type thermocouple. The temperature was calibrated using phases with known melting points, and the reported temperatures are precise to within $\pm 5^\circ$.

The unit-cell parameters were measured from RT to 500°C in steps of 25°C. At each temperature the orientation matrix was updated by centring 24

reflections selected in the range ~ 6.8 – $17.7^\circ \theta$, and accurate lattice parameters (reported in Table 1) were derived from a least-squares procedure based on the Philips *LAT* routine over 27 to 33 d^* spacings, each measured from the positions of all reflection pairs in the range 3 – $26^\circ \theta$.

Datasets of intensities for the structure refinements were collected at $T = 25, 100, 200, 300, 400, 450$ and 500°C . For each dataset a half sphere of intensity data ($\pm h, \pm k, +l$) was collected using $\omega/2\theta$ scans ($2.1^\circ \theta$ scan width; $0.07^\circ \theta \text{ s}^{-1}$ scan speed) in the 2 – $30^\circ \theta$ range for the ambient dataset and 2 – $26.5^\circ \theta$ range for the HT datasets (where the available θ range is limited by the furnace geometry). Raw intensities of reflections were obtained by measuring step-scan profiles and integrating by the Lehman and Larsen (1974) σ_f/I method, as modified by Blessing *et al.* (1974). The intensities of three standard reflections were monitored every 200 measured reflections. No significant variation in beam intensity was registered throughout the experiments, except for the dataset collected at 500°C . In this case, due to deterioration of the crystal due to incipient dehydroxylation, standard intensity decay throughout the data acquisition time was 8.8%

TABLE 1. Unit-cell parameters of alunite at different temperatures.

T ($^\circ\text{C}$)	a (Å)	c (Å)	V (Å ³)
25	6.9749 (6)	17.315 (4)	729.5 (3)
50	6.9750 (6)	17.321 (4)	729.8 (3)
75	6.9758 (6)	17.343 (4)	730.9 (3)
100	6.9771 (7)	17.360 (4)	731.9 (3)
125	6.9779 (6)	17.377 (3)	732.8 (3)
150	6.9786 (5)	17.398 (3)	733.8 (3)
175	6.9794 (6)	17.411 (3)	734.5 (3)
200	6.9806 (7)	17.425 (3)	735.3 (3)
225	6.9814 (5)	17.446 (3)	736.4 (3)
250	6.9824 (6)	17.464 (3)	737.4 (3)
275	6.9859 (6)	17.482 (2)	738.8 (2)
300	6.9859 (5)	17.481 (3)	738.8 (2)
325	6.9875 (5)	17.519 (3)	740.8 (3)
350	6.9876 (6)	17.545 (3)	741.9 (3)
375	6.9895 (7)	17.559 (3)	742.9 (3)
400	6.9897 (6)	17.574 (3)	743.6 (2)
425	6.9911 (5)	17.595 (3)	744.7 (3)
450	6.9916 (7)	17.621 (2)	746.0 (2)
475	6.9921 (7)	17.638 (4)	746.8 (3)
500	6.9935 (7)	17.640 (12)	747.2 (7)

Standard deviations are given in parentheses.

and hence data were scaled accordingly. Intensities were then corrected for Lorentz and polarization effects, and for absorption using the ψ -scan method of North *et al.* (1968). Relevant parameters on data collection are reported in Table 2.

Structure refinements

All structure refinements were carried out in space group $R\bar{3}m$ by full-matrix least-squares methods using *SHELXL-97* (Sheldrick, 1998). Equivalent reflections were averaged, and the resulting internal agreement factors R_{int} are reported in Table 2 for all datasets. Atom-scattering curves for neutral atoms were taken from *International Tables for X-ray Crystallography* (Ibers and Hamilton, 1974). Structure refinement from data collected at RT was performed starting from the model of Menchetti and Sabelli (1976), whereas those from data collected at HT were carried out starting from the model obtained at the immediately lower temperature. On the basis of the chemical analysis and of the thermal behaviour shown by the sample, the possible presence of oxonium (or, more specifically, hydronium) ions, H_3O^+ , at the *A* site was taken into account. It is worth noting that the presence of H_3O^+ ions at the *A* site in potassium-bearing alunite is quite common and is reported by Schukow *et al.* (1999) and Majzlan *et al.* (2006). Refinements were carried out according to the following scheme.

(1) All datasets were initially refined with only K at the *A* site, and the site-occupancy was refined without constraints. This allowed the mean atomic number (m.a.n.) at the site and its variation with increasing temperature to be determined. This is indicative of possible loss of oxonium ions. For this series of refinements, in order to guarantee internal consistency among the data, structure refinement from data collected at RT was performed on a set of data limited to $26.5^\circ \theta$.

(2) Three scattering curves were then refined at the *A* site (K, Na and O for the oxonium ions) for the dataset collected at RT. The sum of occupancies was constrained to 1. The starting value of oxygen occupancy was determined by the variation of m.a.n. detected during the first series of refinements for datasets collected at $T > 200^\circ\text{C}$ and put in the refinement with a soft constraint (estimated standard deviation set to 0.03). In the first stages of this refinement, several cycles were carried out keeping one of the occupancy factors fixed in alternate cycles to avoid correlations. Final refinement converged to K 0.876(4), Na 0.071(8), O 0.053(7).

(3) Occupancy factors for K and Na were then kept fixed to these values in all other refinements. Oxygen occupancy at the *A* site was refined without constraints, thus allowing vacancies at the site. Starting from data collected at 300°C the oxygen occupancy at the *A* site converged to zero, and it was therefore removed from the list.

TABLE 2. Details of data collection and structure refinements for alunite.

	RT	100°C	200°C	300°C	400°C	450°C	500°C
Reflns measured	1442	1066	1066	1074	1078	1081	1086
Reflns unique	292	219	219	221	221	222	223
Average $I/\sigma(I)$	73.53	43.48	66.23	51.28	51.02	44.44	10.22
R_{int} (%)	2.28	4.08	2.76	3.24	3.50	3.66	9.01
Reflns with $I > 2\sigma_I$	274	195	195	197	199	198	163
R_1^* (%)	1.91	2.33	2.30	2.32	2.31	2.60	7.39
R_{all} (%)	2.13	2.83	2.83	2.88	2.84	3.43	11.04
wR_2 (%)	5.78	5.89	7.58	5.92	6.01	6.81	22.56
GOF [†]	1.160	1.262	1.233	1.160	1.260	1.204	1.124
max $\Delta\rho$ ($\text{e } \text{\AA}^{-3}$)	0.34	0.39	0.30	0.26	0.34	0.43	1.53
min $\Delta\rho$ ($\text{e } \text{\AA}^{-3}$)	-0.48	-0.42	-0.49	-0.53	-0.54	-0.57	-0.64

* $R = \sum ||F_o| - |F_c|| / \sum |F_o|$ [R_1 is calculated on reflections with $I > 2\sigma(I)$].

† GOF = $S = [\sum [w(F_o^2 - F_c^2)^2] / (n - p)]^{0.5}$, where n is the number of reflections and p is the total number of parameters refined.

Standard deviations are given in parentheses.

For all structure refinements, all non-hydrogen atoms were refined anisotropically. The hydrogen position of the hydroxyl groups (O3) was located in the difference-Fourier map and inserted in the refinement with isotropic displacement parameters. On the basis of neutron diffraction data both on alunite (Schukow *et al.*, 1999) and jarosite (Xu *et al.*, 2010), a soft constraint was used for the O–H distance (0.9 Å with an estimated standard deviation of 0.02). Despite the lower resolution of the datasets collected at HT, the hydrogen position of hydroxyl groups was still evident in the difference-Fourier maps up to 450°C. It should be noted that the hydrogen atoms of the oxonium ions were not located [attempts of localizing them were not successful even by neutron diffraction (Schukow *et al.*, 1999)]. As the trivalent cation site in alunite-group minerals is commonly partly vacant (Stoffregen *et al.*, 2000; Majzlan *et al.*, 2006), the Al occupancy was refined without constraints.

Structure factors were weighted according to $w = 1/[\sigma^2(F_o^2) + (AP)^2 + BP]$, where $P = (F_o^2 + 2 F_c^2)/3$, and A and B were chosen for every crystal to produce a flat analysis of variance in terms of F_c^2 as suggested by the program. An extinction parameter was refined to correct the structure factors according to the equation $F_o = F_c k [1 + 0.001x F_c^2 \lambda^3 / \sin 2\theta]^{-1/4}$ (where k is the overall scale factor). All parameters were refined simultaneously. Final difference-Fourier maps were featureless except for the dataset collected at 500°C. In this case, a few peaks were present ($1.53 \text{ e}^- \text{ \AA}^{-3}$ at 0.66 Å from K; $0.93 \text{ e}^- \text{ \AA}^{-3}$ at 0.95 Å from O1) but were not included in the model. Details of the structure refinements are given in Table 2. Fractional coordinates and displacement parameters are reported in Table 3 and interatomic distances and selected geometrical parameters are reported in Table 4. The CIF files and lists of observed and calculated structure factors have been deposited with the Principal Editors of *Mineralogical Magazine* and are available at www.minersoc.org/pages/e-journals/dep_mat_mm.html.

Results and discussion

Thermal expansion

In Fig. 2, the variations of unit-cell parameters and volume, normalized to their RT values, are reported as a function of temperature in the range 25–500°C. The crystal under investigation began to deteriorate at 500°C and this is consistent with previous thermal analyses of potassium-bearing

alunite (e.g. Rudolph *et al.*, 2003; Kristóf *et al.*, 2010, and references therein). At higher temperatures only broad and weak diffraction effects due to polycrystalline material were observed and therefore the experiment was stopped and the residual crystal recovered for EDS analysis. It is evident from Fig. 2 that alunite expands anisotropically: it is almost rigid on the (0001) plane, with most of the contribution to volume dilatation coming from expansion along the c direction. This behaviour is consistent with the layered nature of the crystal structure, which is made up of $\text{Al}(\text{O},\text{OH})_6$ and SO_4 units held together by relatively weak interlayer interactions, and is in agreement with the elastic properties determined by Brillouin spectroscopy (Majzlan *et al.*, 2006). Unit-cell parameters and volume-expansion curves of alunite were fitted using a linear model, as the spread of data did not justify the use of more sophisticated T -dependent models (Berman, 1988; Fei, 1995; Holland and Powell, 1998). The linear thermal expansion coefficients, determined in the temperature range 50–475°C (lower and upper limits excluded in the calculation) by least-squares regression analysis, are $\alpha_a = 0.61(2) \times 10^{-5} \text{ K}^{-1}$ ($R^2 = 0.988$), $\alpha_c = 4.20(7) \times 10^{-5} \text{ K}^{-1}$ ($R^2 = 0.996$), ratio $\alpha_c/\alpha_a = 6.89$, $\alpha_v = 5.45(7) \times 10^{-5} \text{ K}^{-1}$ ($R^2 = 0.998$). These values are very close to those measured by *in situ* neutron diffraction by Xu *et al.* (2010) for deuterated jarosite, $\text{KFe}_3(\text{SO}_4)_2(\text{OD})_6$, in the temperature range 25–300°C, i.e. up to the collapse of the jarosite crystal structure. Alunite and jarosite have the same expansion coefficient along the c axis, and the alunite expansion

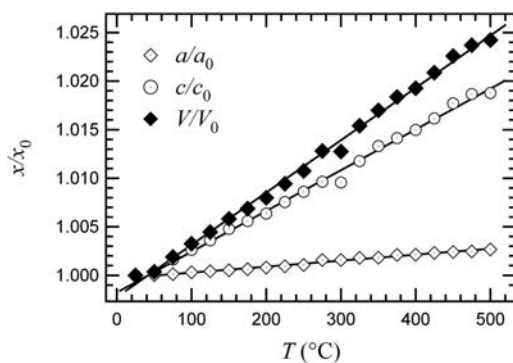


FIG. 2. Relative variations with T of the unit-cell parameters and unit-cell volume of alunite, normalized to their RT values. Linear regressions calculated in the range 50–475°C are shown as solid lines.

TABLE 3. Fractional coordinates and anisotropic displacement parameters, U_{ij} ($\text{\AA}^2 \times 10^3$), for alunite.

T ($^{\circ}\text{C}$)	25	100	200	300	400	450	500
Site A ($0.876 \text{ K}^+ + 0.071 \text{ Na}^+ + x \text{ H}_3\text{O}^+$), Wyckoff position $3a$ (0,0,0)							
Occ. O	0.053(7)	0.049(9)	0.039(9)	–	–	–	–
U_{11}	14(1)	17(1)	23(1)	27(1)	32(1)	35(1)	29(2)
U_{33}	10(1)	12(1)	15(1)	17(1)	20(1)	23(1)	42(5)
U_{12}	7(1)	9(1)	11(1)	13(1)	16(1)	17(1)	14(1)
U_{eq}	13(1)	16(1)	20(1)	23(1)	28(1)	31(1)	33(2)
Site Al, Wyckoff position $9d$ (0,1/2,1/2)							
Occ. Al	0.988(4)	0.975(7)	0.972(7)	0.963(6)	0.964(7)	0.972(7)	0.932(18)
U_{11}	4(1)	4(1)	6(1)	7(1)	8(1)	9(1)	11(2)
U_{22}	5(1)	6(1)	7(1)	9(1)	10(1)	11(1)	13(2)
U_{33}	9(1)	10(1)	12(1)	14(1)	17(1)	19(1)	54(4)
U_{12}	0(1)	2(1)	3(1)	3(1)	4(1)	5(1)	5(1)
U_{13}	0(1)	0(1)	0(1)	0(1)	0(1)	0(1)	1(2)
U_{23}	2(1)	0(1)	0(1)	0(1)	0(1)	0(1)	1(1)
U_{eq}	6(1)	7(1)	8(1)	10(1)	12(1)	13(1)	26(2)
Site S, Wyckoff position $6c$ (0,0, z)							
z/c	0.30282(4)	0.30257(6)	0.30215(7)	0.30179(6)	0.30142(7)	0.30118(7)	0.3010(3)
U_{11}	6(1)	8(1)	10(1)	12(1)	14(1)	16(1)	19(1)
U_{33}	7(1)	9(1)	9(1)	11(1)	15(1)	16(1)	51(3)
U_{12}	3(1)	4(1)	5(1)	6(1)	7(1)	7(1)	9(1)
U_{eq}	6(1)	8(1)	10(1)	12(1)	14(1)	15(1)	30(1)
Site O1, Wyckoff position $6c$ (0,0, z)							
z/c	0.38666(12)	0.38589(19)	0.38517(20)	0.38430(20)	0.38341(20)	0.38311(21)	0.3827(8)
U_{11}	13(1)	16(1)	21(1)	25(1)	29(1)	30(1)	35(4)
U_{33}	7(1)	9(2)	9(2)	11(2)	14(1)	17(2)	53(9)
U_{12}	7(1)	8(1)	10(1)	13(1)	15(1)	15(1)	18(2)
U_{eq}	11(1)	13(1)	17(1)	21(1)	24(1)	26(1)	41(3)
Site O2, Wyckoff position $18h$ ($x, -x, z$)							
x/a	0.21823(10)	0.21840(17)	0.21847(18)	0.21854(17)	0.21866(17)	0.21872(18)	0.2186(6)
z/c	-0.05997(6)	-0.06021(10)	-0.06042(11)	-0.06078(11)	-0.06115(11)	-0.06135(12)	-0.0619(4)
$U_{11} = U_{22}$	11(1)	13(1)	17(1)	20(1)	24(1)	25(1)	32(3)
U_{33}	10(1)	12(1)	14(1)	16(1)	20(1)	23(1)	48(5)
U_{12}	8(1)	10(1)	12(1)	14(1)	17(1)	18(1)	21(3)
$U_{13} = U_{23}$	0(1)	0(1)	1(1)	0(1)	1(1)	1(1)	1(2)
U_{eq}	9(1)	11(1)	14(1)	17(1)	21(1)	22(1)	35(2)
Site O3, Wyckoff position $18h$ ($x, -x, z$)							
x/a	0.12604(10)	0.12598(18)	0.12604(20)	0.12611(18)	0.12616(18)	0.12624(19)	0.1266(6)
z/c	0.14024(6)	0.14029(11)	0.14035(12)	0.14039(11)	0.14040(12)	0.14042(12)	0.1403(4)
$U_{11} = U_{22}$	6(1)	7(1)	9(1)	11(1)	13(1)	13(1)	16(2)
U_{33}	12(1)	15(1)	17(1)	20(1)	24(1)	26(1)	67(5)
U_{12}	3(1)	3(1)	4(1)	5(1)	5(1)	5(1)	7(2)
$U_{13} = -U_{23}$	1(1)	1(1)	2(1)	2(1)	2(1)	2(1)	1(2)
U_{eq}	8(1)	10(1)	12(1)	15(1)	17(1)	18(1)	34(2)
Site H, Wyckoff position $18h$ ($x, -x, z$)							
x/a	0.1879(22)	0.1830(28)	0.1835(25)	0.1840(24)	0.1838(25)	0.1837(26)	–
z/c	0.1165(14)	0.1090(22)	0.1108(20)	0.1110(18)	0.1111(20)	0.1104(21)	–
U_{iso}	30(7)	34(16)	37(13)	41(12)	48(13)	61(16)	–

Standard deviations are given in parentheses.

THERMAL EXPANSION OF ALUNITE

TABLE 4. Bond distances (Å) and selected geometrical parameters for alunite.

<i>T</i> (°C)	25	100	200	300	400	450	500
K polyhedron							
K–O2 (× 6)	2.834(1)	2.839(2)	2.843(2)	2.850(2)	2.857(2)	2.861(2)	2.864(7)
K–O3 (× 6)	2.866(1)	2.872(2)	2.881(2)	2.890(2)	2.902(2)	2.909(2)	2.912(7)
<K–O>	2.850(1)	2.855(2)	2.863(2)	2.870(2)	2.879(2)	2.885(2)	2.888(7)
Volume (Å ³)	56.128	56.400	56.748	57.105	57.567	57.822	57.958
Al octahedron							
Al–O2 (× 2)	1.950(1)	1.951(2)	1.954(2)	1.955(2)	1.958(2)	1.960(2)	1.952(7)
Al–O3 (× 4)	1.8751(5)	1.8756(8)	1.8768(9)	1.8786(9)	1.8803(9)	1.8812(9)	1.884(3)
<Al–O>	1.9000(6)	1.901(3)	1.903(1)	1.904(1)	1.906(1)	1.908(1)	1.906(4)
Volume (Å ³)	9.137	9.148	9.176	9.193	9.228	9.245	9.231
OAV	0.905	0.870	0.874	0.837	0.906	0.917	0.952
S tetrahedron							
S–O1	1.452(2)	1.446(4)	1.447(4)	1.442(4)	1.441(4)	1.444(4)	1.441(15)
S–O2 (× 3)	1.481(1)	1.480(2)	1.479(2)	1.480(2)	1.480(2)	1.480(2)	1.484(7)
<S–O>	1.474(1)	1.472(3)	1.471(3)	1.471(3)	1.471(3)	1.471(3)	1.474(9)
Volume (Å ³)	1.643	1.635	1.634	1.632	1.631	1.633	1.642
O1...O2 edge	2.405(2)	2.400(3)	2.399(3)	2.397(3)	2.398(4)	2.400(4)	2.405(16)
O2...O2 edge	2.409(1)	2.406(2)	2.405(2)	2.406(2)	2.405(2)	2.404(2)	2.407(7)
TAV	0.547	0.657	0.551	0.650	0.856	0.918	1.478
Hydrogen bonds O3–H...O1							
O3–H (Å)	0.85(2)	0.88(3)	0.86(3)	0.87(3)	0.87(3)	0.87(3)	–
O3...O1 (Å)	2.922(1)	2.932(2)	2.943(3)	2.955(2)	2.968(3)	2.973(3)	–
H...O1 (Å)	2.07(2)	2.06(3)	2.08(3)	2.09(2)	2.10(3)	2.10(3)	–
O3–H–O1 (°)	177(1)	170(2)	173(2)	174(2)	174(2)	173(2)	–

Standard deviations are given in parentheses.

The abbreviation OAV is octahedral angle variance, TAV is tetrahedral angle variance.

coefficient along *a* is only slightly larger than jarosite, which has $\alpha_a = 0.41 \times 10^{-5} \text{ K}^{-1}$ (Xu *et al.*, 2010). Although the variations are very small, the data of Xu *et al.* (2010) on the *a* cell parameter as a function of *T* in jarosite might be better interpreted using a *T*-dependent model or by hypothesizing a change in the slope at ~150–175°C. The jarosite thermal expansion coefficient along *a* calculated for RT–175°C is the same as for alunite, and this suggests that the particular trivalent octahedral cation in the *R* position has little effect on the thermal expansion behaviour of the structure.

Although all of the linear regressions in Fig. 2 have linear correlation coefficients, R^2 , that are close to unity, a close inspection of the data (Fig. 3), shows a small discontinuity at *T* ~275–300°C, where there is a discontinuous increase of the *a* cell parameter (Fig. 3*a*) and a slight change in the slope of *c* cell parameter *vs.*

temperature curve (Fig. 3*b*). Linear regressions over the two temperature ranges, below and above the discontinuity, are shown in the figure, although differences in the thermal expansion coefficients are very small. No change of symmetry is observed at the discontinuity.

The discontinuity is interpreted on the basis of partial replacement of potassium by oxonium ions at the *A* site. Rudolph *et al.* (2003) showed that the decomposition temperature of alunite is strongly dependent on the cationic species occupying the *A* site, according to the scheme: K^+ (490°C) > Na^+ (480°C) > Rb^+ (420°C) > NH_4^+ (350°C) > H_3O^+ (200°C). Moreover, a strong dependence on the degree of hydroxonium substitution in the members of the $\text{K}_x(\text{H}_3\text{O})_{1-x}\text{Al}_3(\text{SO}_4)_2(\text{OH})_6$ series has been highlighted. Therefore, it can be argued that the alunite sample used in this work probably contained a small quantity of oxonium cations

which were lost before dehydroxylation started, leaving vacancies at the *A* site but not causing the collapse of the crystal structure. This would explain the discontinuity observed in the thermal expansion as well as the decrease in the m.a.n. at the *A* site determined by the structure refinements. Using DTA and DTG analyses, Kristóf *et al.* (2010) detected a thermal effect at 246°C (or 222°C, depending on the heating conditions) in natural potassium alunite, which they interpreted as loss of water according to the formula $\text{KAl}_3(\text{SO}_4)_2(\text{OH})_6 \cdot x(\text{H}_2\text{O}) \rightarrow \text{KAl}_3(\text{SO}_4)_2(\text{OH})_6 + x\text{H}_2\text{O}$. Water in this form has never been

reported in diffraction analyses of alunite, but such evidence highlights the contentious issue of the ‘excess water’ in alunites, which has been discussed by many authors (Härtig *et al.*, 1984; Bohmhammel *et al.*, 1987; Ripmeester *et al.*, 1986). The excess water is likely to be adsorbed or ‘trapped’ water which is not part of the stoichiometry of alunite. The presence of oxonium in the natural samples of Kristóf *et al.* (2010) only partially explains the measured weight loss. Unfortunately, the alunite specimen from Hungary used in the present HT structural investigation consists of only a few crystals and hence not enough material is available for additional thermal analyses. The hypothesis that the sample is characterised by partial $\text{K}^+/\text{H}_3\text{O}^+$ substitution is nonetheless supported by the results of the structural investigation, which shows a loss of electrons at the *A* site at HT.

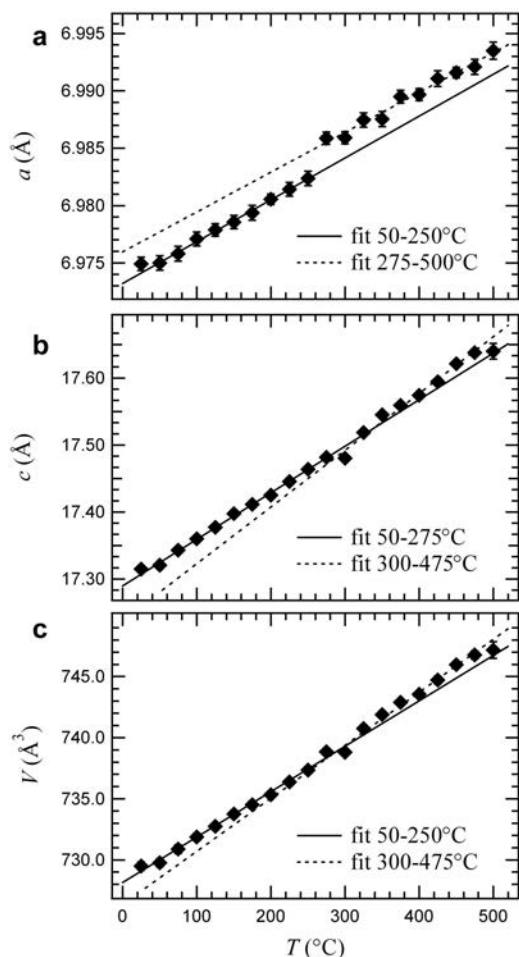


FIG. 3. The unit-cell parameters, *a* and *c*, and unit-cell volume, *V*, of alunite plotted as a function of temperature: (a) *a* vs. *T*; (b) *c* vs. *T*; (c) *V* vs. *T*. Linear regressions in the two temperature ranges above and below the discontinuity are shown.

Structural variations at high temperature

The thermal behaviour of alunite, the anisotropy of its axial thermal expansion coefficients in the temperature range investigated and the discontinuity detected in the plots of unit-cell parameters vs. temperature at ~275–300°C are hereafter rationalized in terms of polyhedral expansion and interconnectivity.

As stated above, most of the alunite structure dilatation as a function of temperature is related to expansion along the *c* axis. This results principally from the expansion of the K polyhedra, as is evident from Fig. 4, where variations of individual and mean K–O distances are plotted. The

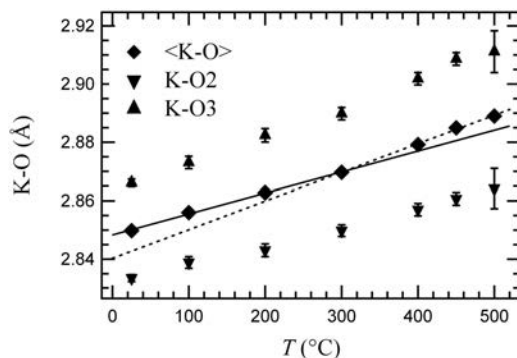


FIG. 4. Individual and mean K–O bond lengths as a function of temperature. Linear regressions calculated through points that are above and below the discontinuity are shown.

linear polyhedral expansion coefficient, calculated across the whole T range investigated, is $8.01(3) \times 10^{-5} \text{ K}^{-1}$ ($R^2 = 0.992$). There is a slight change of slope at $T = 300^\circ\text{C}$. This discontinuity can be interpreted on the basis of a loss of oxonium ions with the formation of vacancies at the A site.

The individual and average Al–O bond distances are plotted as a function of temperature in Fig. 5. The $\text{Al}(\text{O},\text{OH})_6$ octahedral network is relatively rigid; its linear average polyhedral expansion coefficient across the whole temperature range is $1.8(1) \times 10^{-5} \text{ K}^{-1}$ ($R^2 = 0.992$).

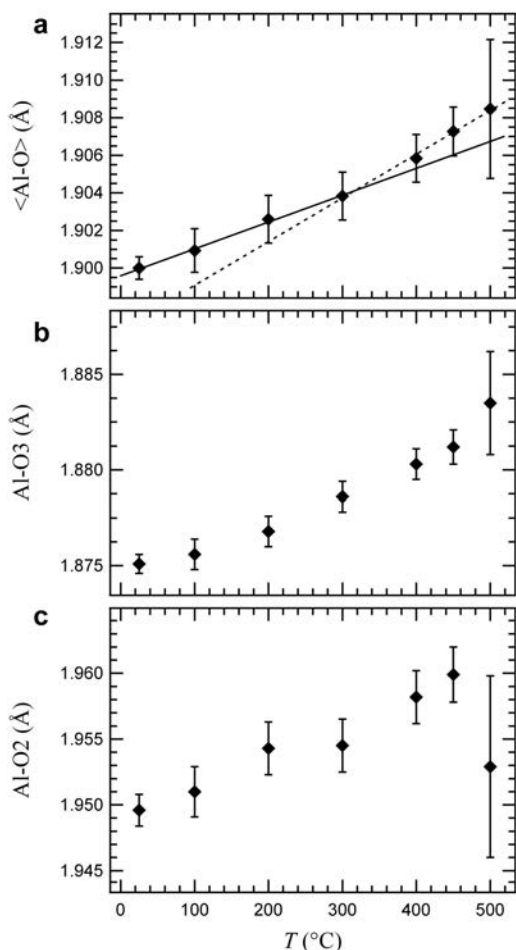


FIG. 5. Individual and mean Al–O bond lengths as a function of temperature: (a) $\langle \text{Al–O} \rangle$ vs. T ; (b) Al–O3 vs. T ; (c) Al–O2 vs. T . Linear regressions calculated through point that are above and below the discontinuity are shown for the mean Al–O distance.

The discontinuity at $T = 300^\circ\text{C}$ is evident. Most of the contribution to polyhedral expansion is produced by the lengthening of the Al–O2 distance, i.e. the bond to the oxygen atom that is shared with the sulfate tetrahedron, whose direction vector has its major component along c . The Al–O2 distance increases almost twice as much as the Al–O3 distance, i.e. that to the hydroxyl group shared with an adjacent Al octahedron to form the network along the (0001) basal plane described above (Fig. 1b). Moreover, the Al–O3 distance starts to increase only at $T > 200^\circ\text{C}$. Overall, the $\text{Al}(\text{O},\text{OH})_6$ octahedron become more elongated along the c axis with increasing temperature.

The bond distances of the sulfate tetrahedron are reported in Fig. 6. A slight contraction of the tetrahedron is observed with increasing temperature up to $\sim 300^\circ\text{C}$, when a plateau is reached and the tetrahedron seems not to be sensitive to further increases in temperature. The contraction seems to be mostly due to a shortening of the apical S–O1 distance, where O1 is the unshared

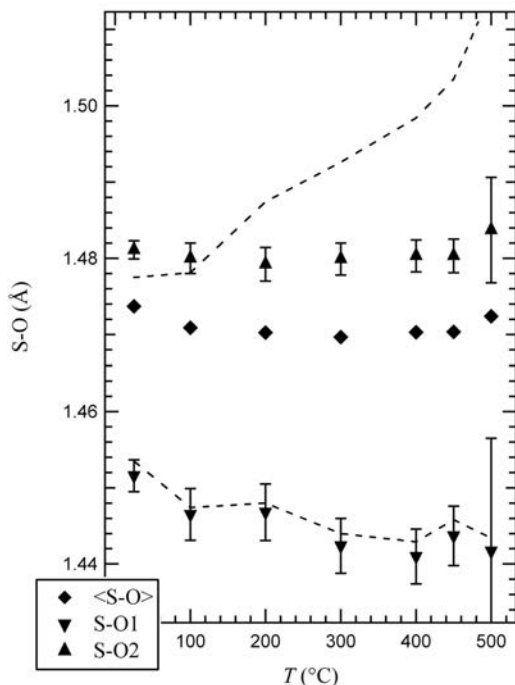


FIG. 6. Individual and mean S–O bond lengths as a function of temperature. Dashed lines represent the upper and lower limits of S–O1 bond distances corrected for thermal motion.

oxygen atom which acts as an acceptor for H-bonds. This behaviour is also evident if the S–O1 bond distances are corrected for thermal motion. The interatomic distances measured by XRD are typically underestimates and appropriate corrections, which require the use of accurate anisotropic displacement parameters (ADPs) must be applied. To perform a general correction for thermal motion, the ADPs and the correlation tensors must be known; these cannot be directly determined from Bragg-diffraction measurements, although they can, in principle, be obtained by lattice dynamic calculations. Without assuming any specific vibrational model (e.g. rigid body, riding or uncorrelated motion), bond distances cannot be corrected for thermal motion; nonetheless an estimate of the possible errors, i.e. an upper and a lower limit for the corrected interatomic distances, can be obtained (Busing and Levy, 1964; Johnson, 1970*a,b*; Scheringer, 1972). Such values are reported in Fig. 6 for the S–O1 distances and they confirm that a slight contraction of the tetrahedron is theoretically possible up to $T = 300^\circ\text{C}$. The sulfate tetrahedron maintains its shape almost unchanged in the temperature range 25–300°C, but at higher temperatures it is significantly distorted. This is evident from Fig. 7, where the tetrahedral angle variance (Robinson *et al.*, 1971) is reported as a function of temperature and compared with the octahedral angle variance relative to Al coordination, which unlike the tetrahedral angle, does not change significantly.

Increasing temperature causes the $\text{Al}(\text{O},\text{OH})_6$ sheets to move further apart, and this results in an

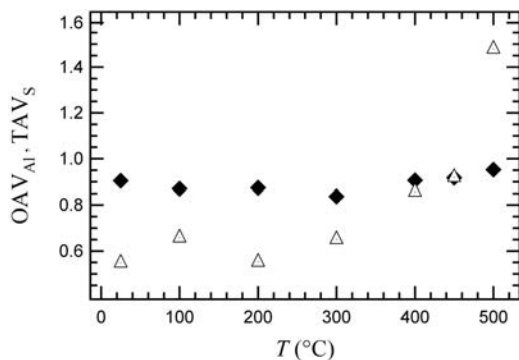


FIG. 7. Polyhedral distortion parameters as a function of temperature. Diamonds represent octahedral angle variance (OAV) for Al; triangles represent tetrahedral angle variance (TAV) for S.

expansion of the coordination polyhedron around the intercalated potassium cation. In particular, the K–O3 distances, where O3 represents the oxygen atoms of the basal plane of Al octahedra, expand much more than the shorter K–O2 distances (Fig. 4). In the structure, three adjacent Al octahedra are inclined one to the other so that their apical oxygen atoms O2 form the three basal edges of sulfate tetrahedra (Fig. 1*b*). A lengthening of Al–O2 distances is accommodated by a contraction of the O2–O2 edges of the sulfate tetrahedra (Table 4). As a consequence the sulfur atom moves towards the O1 apical oxygen atom, resulting in a shortening of the S–O1 distance and a slight overall contraction of the tetrahedron volume, with no significant change in its degree of distortion. At higher temperatures, the tetrahedron does not change in volume but becomes more and more distorted, the Al octahedron starts expanding on the (0001) plane and, consequently, a change of slope in the lengthening of K–O3 bond distance is also observed.

References

- Ballhorn, R., Brunner, H. and Schwab, R.G. (1989) Artificial compounds of the crandallite type: a new material for separation and immobilization of fission products. *Scientific Basis for Nuclear Waste Management*, **12**, 249–252.
- Bayliss, P., Kolitsch, U., Nickel, E.H. and Pring, A. (2010) Alunite supergroup: recommended nomenclature. *Mineralogical Magazine*, **74**, 919–927.
- Berman, R.G. (1988) Internally-consistent thermodynamic data for minerals in the system $\text{Na}_2\text{O}-\text{K}_2\text{O}-\text{CaO}-\text{MgO}-\text{FeO}-\text{Fe}_2\text{O}_3-\text{Al}_2\text{O}_3-\text{SiO}_2-\text{TiO}_2-\text{H}_2\text{O}-\text{CO}_2$. *Journal of Petrology*, **29**, 445–522.
- Blessing, R.H., Coppens, P. and Becker, P. (1974) Computer analysis of step-scanned X-ray data. *Journal of Applied Crystallography*, **7**, 488–492.
- Bohmhammel, K., Naumann, R. and Paulik, F. (1987) Thermoanalytical and calorimetric investigations on the formation and decomposition of some alunites. *Thermochimica Acta*, **121**, 109–119.
- Busing, W.R. and Levy, H.A. (1964) The effect of thermal motion on the estimation of bond lengths from diffraction measurements. *Acta Crystallographica*, **17**, 142–146.
- Dill, H.G. (2001) The geology of aluminium phosphates and sulphates of the alunite group minerals: a review. *Earth Science Reviews*, **53**, 35–93.
- Fei, Y. (1995) Thermal expansion. Pp. 29–44 in: *AGU Reference Shelf 2: Mineral Physics and Crystallography – a Handbook of Physical*

- Constants* (T.J. Ahrens, editor). American Geophysical Union, Washington DC.
- Fink, W.L., Van Horn, K.R. and Pazour, H.A. (1931) Thermal decomposition of alunite. *Industrial and Engineering Chemistry*, **23**, 1248–1250.
- Härtig, C., Brand, P. and Bohmhammel, K. (1984) Fe-Al-Isomorphie und Strukturwasser in Kristallen vom Jarosit-Alunit-Type. *Zeitschrift für anorganische und allgemeine Chemie*, **508**, 159–164.
- Hendricks, S.B. (1937) The crystal structures of alunite and the jarosites. *American Mineralogist*, **22**, 773–784.
- Holland, T.J.B. and Powell, R. (1998) An internally consistent thermodynamic data set for phases of petrological interest. *Journal of Metamorphic Geology*, **16**, 309–343.
- Ibers, J.A. and Hamilton, W.C. (1974) *International Tables for X-ray Crystallography*. Kynoch Press, Birmingham, UK.
- Jambor, J.L. (1999) Nomenclature of the alunite supergroup. *The Canadian Mineralogist*, **37**, 1323–1341.
- Johnson, C.K. (1970a) Generalized treatments for thermal motion. Pp. 132–160 in: *Thermal Neutron Diffraction* (B.T.M. Willis, editor). Oxford University Press, Oxford, UK.
- Johnson, C.K. (1970b) An introduction to thermal motion analysis. Pp. 220–226 in: *Crystallographic Computing* (F.R. Ahmed, editor). Munksgaard, Copenhagen, Denmark.
- Katsioti, M., Boura, P., Agatzini, S., Tsakiridis, P.E. and Oustadakis, P. (2005) Use of jarosite/alunite precipitate as a substitute for gypsum in Portland cement. *Cement and Concrete Composites*, **27**, 3–9.
- Kolitsch, U., Tiekink, E.R.T., Slade, P.G., Taylor, M.R. and Pring, A. (1999) Hinsdalite and plumbogummite, their atomic arrangements and disordered lead sites. *European Journal of Mineralogy*, **11**, 513–520.
- Kristóf, J., Frost, R.L., Palmer, S.J., Horváth, E. and Jakab, E. (2010) Thermoanalytical studies of natural potassium, sodium and ammonium alunites. *Journal of Thermal Analysis and Calorimetry*, **100**, 961–966.
- Lehman, M.S. and Larsen, F.K. (1974) A method for location of the peaks in step-scan measured Bragg reflections. *Acta Crystallographica*, **A30**, 580–584.
- Majzlan, J., Speziale, S., Duffy, T.S. and Burns, P.C. (2006) Single-crystal elastic properties of alunite, $\text{KAl}_3(\text{SO}_4)_2(\text{OH})_6$. *Physics and Chemistry of Minerals*, **33**, 567–573.
- Menchetti, S. and Sabelli, C. (1976) Crystal chemistry of the alunite series: crystal structure refinement of alunite and synthetic jarosite. *Neues Jahrbuch für Mineralogie, Monatshefte*, **H9**, 406–417.
- Mills, S.J., Hatert, F., Nickel, E.H. and Ferraris, G. (2009) The standardisation of mineral group hierarchies: application to recent nomenclature proposals. *European Journal of Mineralogy*, **21**, 1073–1080.
- North, A.C.T., Phillips, D.C. and Mathews, F.S. (1968) A semi-empirical method of absorption correction. *Acta Crystallographica*, **A24**, 351–359.
- Özacar, M. (2003) Phosphate adsorption characteristics of alunite to be used as a cement additive. *Cement and Concrete Research*, **33**, 1583–1587.
- Ripmeester, J.A., Ratcliffe, Ch.I., Dutrizac, J.E. and Jambor, J.L. (1986) Oxonium in the alunite-jarosite group. *The Canadian Mineralogist*, **23**, 435–447.
- Robinson, K., Gibbs, G.V. and Ribbe, P.H. (1971) Quadratic elongation, a quantitative measure of distortion in co-ordination polyhedra. *Science*, **172**, 567–570.
- Rudolph, W.W., Mason, R. and Schmidt, P. (2003) Synthetic alunites of the potassium-oxonium solid solution series and some other members of the group: synthesis, thermal and X-ray characterization. *European Journal of Mineralogy*, **15**, 913–924.
- Scheringer, C. (1972) A lattice dynamical treatment of the thermal motion bond-length correction. *Acta Crystallographica*, **A28**, 616–619.
- Schukow, H., Breiting, D.K., Zeiske, T., Kubanek, F., Mohr, J. and Schwab, R.G. (1999) Localization of hydrogen and content of oxonium cations in alunite via neutron diffraction. *Zeitschrift für Anorganische und Allgemeine Chemie*, **625**, 1047–1050.
- Sengil, I.A. (1995) The utilization of alunite ore as a coagulant aid. *Water Research*, **29**, 1988–1992.
- Sheldrick, G.M. (1998) *SHELX97 – Programs for Crystal Structure Analysis (Release 97-2)*. Institut für Anorganische Chemie der Universität, Göttingen, Germany.
- Stoffregen, R.E. and Alpers, C.N. (1992) Observations on the unit cell parameters, water contents and δD of natural and synthetic alunites. *American Mineralogist*, **77**, 1092–1098.
- Stoffregen, R.E., Alpers, C.N. and Jambor, J.L. (2000) Alunite-jarosite crystallography, thermodynamics, and geochronology. Pp. 453–479 in: *Sulfate Minerals: Crystallography, Geochemistry, and Environmental Significance* (C.N. Alpers, J.L. Jambor and D.K. Nordstrom, editors). Reviews in Mineralogy and Geochemistry, **40**. Mineralogical Society of America, Washington DC and the Geochemical Society, St Louis, Missouri, USA.
- Xu, H., Zhao, Y., Vogel, S.C., Hickmott, D.D., Daemen, L.L. and Hartl, M.A. (2010) Thermal expansion and decomposition of jarosite: a high-temperature neutron diffraction study. *Physics and Chemistry of Minerals*, **37**, 73–82.
- Wang, R., Bradley, W.F. and Steinfink, H. (1965) The crystal structure of alunite. *Acta Crystallographica*, **18**, 249.